Radiative decay from the 2^3P_2 and 2^3P_0 levels of heliumlike argon

William A. Davis and Richard Marrus
Materials and Molecular Research Division, Lawrence Berkeley Laboratory and Department of Physics, University of California, Berkeley, California 94720
(Received 22 November 1976)

The allowed electric dipole transitions 2^3P_2-2^3S_1 and 2^3P_0-2^3S_1 in heliumlike argon (Ar^{+16}) have been observed in a foil-excited beam with a vacuum-ultraviolet monochromator. The wavelengths of these transitions were measured, and the lifetimes of the excited states determined by a time-of-flight technique. The results are $\lambda(2^3P_2\text{-}2^3S_1) = 560.2 \pm 0.9$ Å, $\lambda(2^3P_0\text{-}2^3S_1) = 660.7 \pm 1.1$ Å, $\tau(2^3P_2) = 1.62 \pm 0.08 \times 10^{-9}$ sec, and $\tau(2^3P_0) = 4.87 \pm 0.44 \times 10^{-9}$ sec.

I. INTRODUCTION

The study of the atomic properties of the two-electron atom is a program that has continued to be of intense research interest for over 100 years. In 1910, for example, Kayser[1] compiled a bibliography of 120 references for the spectrum of helium, and in the 1970's much new work continues.[2]

In this paper we concern ourselves with the transitions 2^3P_2-2^3S_1 and 2^3P_0-2^3S_1 in heliumlike argon ($Z=18$). Interest in the fine structure of the $n=2$ state comes from the fact that this splitting is determined mainly by the electron-electron interaction, relativistic effects, and quantum electrodynamic corrections. Moreover, the strong Z dependence of these latter effects makes it possible to study aspects of these interactions which are below the limit of detection in helium itself. As an example, in heliumlike argon, quantum electrodynamic effects (principally the Lamb shift) contribute roughly 1% of the 2^3P_J-2^3S_1 transition energy, compared to only 2×10^{-5} in helium itself.

Highly ionized spectra of ions above $Z=10$ are not well known because of difficulties in excitation and analysis of the spectra. Much of the reported work has been limited to the x-ray spectrum, composed mainly of resonance lines.[3] In this work, we use beam-foil excitation to populate the 2^3P_J levels in heliumlike argon (see Fig. 1). These transitions fall in the vacuum ultraviolet near 600 Å. They should also be observable from astrophysical and plasma sources.

II. PREVIOUS WORK

A. Energy calculations

The fine structure of the helium atom was first calculated by Heisenberg in 1926 using a semiclassical spin-spin interaction.[4] Subsequent calculations have evaluated the relativistic retarded interaction of the two electrons, correlation effects, and quantum electrodynamic (QED) contributions. At present the most precise calculation is the 2^3P_0-2^3P_1 energy splitting to an accuracy of 1.44 ppm.[5] Comparison with the best experimental results, accurate to 1.2 ppm,[6] yields a value for the fine-structure constant α good to 0.94 ppm.

Study of the fine structure of the 2^3P_J states in high-Z heliumlike atoms requires observation of decays from the 2^3P_J states to the 2^3S_1 state. Calculations of the 2^3P_J-2^3S_1 energy differences are more difficult because of the need to include non-spin-dependent operators.

Energy calculations in high-Z ions are generally expressed as power series in two parameters, $1/Z$ and $(Z\alpha)^2$. Higher-order relativistic terms involve higher powers of $(Z\alpha)^2$. Terms involving $(1/Z)^n$ represent n-photon exchange effects of the two electrons. To this perturbation scheme must be added terms for mass corrections, nuclear volume corrections, and QED effects.

The nonrelativistic terms of order $(1/Z)^n(Z\alpha)^2$ for all $n \geq 0$, have been calculated using a perturbation-variation scheme by Sandars and Scherr,[7] and strictly variationally by Accad, Pekeris, and Schiff[8] (APS) for ions of $2 \leq Z \leq 10$. Using the nonrelativistic wave functions which they derived, APS evaluated the Breit operators to first order and thereby calculated the contributions of order $(Z\alpha)^4$

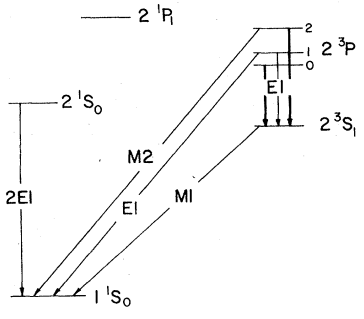

FIG. 1. Decay modes of the metastable $n=2$ states of heliumlike ions.

TABLE I. Magnitudes of the various contributing terms to the $2\,^3P_J \rightarrow 2\,^3S_1$ energy for He-like argon are shown for the two observed transitions.

Contribution	Order	Value (eV) $2\,^3P_0$-$2\,^3S_1$	Value (eV) $2\,^3P_2$-$2\,^3S_1$
Nonrelativistic, [a,b] all orders in $1/Z$	$(Z\alpha)^2$, $(1/Z\alpha)^2$, ...	17.7997	17.7997
Relativistic hydrogenic [c]	$(Z\alpha)^4$	0.0	4.7536
Breit interaction (Doyle) [d]	$(1/Z)(Z\alpha)^4$	1.2071	−0.3067
Mohr—extrap. [e]	$(1/Z^2)(Z\alpha)^4$	−0.124	+0.0009
Relativistic hydrogenic [c]	$(Z\alpha)^6$	0.0	0.0513
One-photon exchange-Mohr [e]	$(1/Z)(Z\alpha)^6$	0.015	•••
Hydrogenic Lamb shift [f]	$\alpha(Z\alpha)^4$, and higher order in $(Z\alpha)$	−0.161	−0.151
Mass polarization [g]		−0.0086	−0.0086
(reduced mass effect)		< 0.0003	< 0.0003
		18.73 ± 0.03 eV	22.14 ± 0.03 eV
	or	662.0 ± 1.1 Å	560.0 ± 0.9 Å

[a] Reference 7.
[b] Reference 8.
[c] Reference 11.
[d] Reference 12.
[e] Reference 10.
[f] Reference 21.
[g] Reference 15.

to all orders in $1/Z$ for ions with $2 \leq Z \leq 10$.[8] The results of APS have been extended to ions above $Z = 10$ by Ermolaev and Jones using rational interpolation functions.[9]

The no-photon exchange terms to all orders in $(Z\alpha)^2$ can be obtained from the Dirac equation for hydrogen. Using wave functions which are products of Dirac hydrogenic wave functions, Mohr[10] numerically evaluated the relativistic one-photon exchange operator[11] to all orders in $(Z\alpha)^2$. By assuming terms of order $(1/Z)(Z\alpha)^2$ (Ref. 7) and $(1/Z)(Z\alpha)^4$ (Ref. 12) are known he has extrapolated the term of order $(1/Z)(Z\alpha)^6$. Ermolaev and Jones[13] observed that the major effect of second-order corrections[14] is accounted for by including the mixing of the $n\,^1P_1$ and $n\,^3P_1$ levels. This was verified by Schiff, Accad, and Pekeris.[15] These terms enter to order $(1/Z^2)(Z\alpha)^6$ or higher order and only affect the location of the $^3P_1$ level, not the $^3P_0$ and $^3P_2$ levels.

For light ions the largest part of the mass correction is the normal, or reduced mass correction. The nonseparability of the nonrelativistic Schrödinger equation for a two-electron atom is accounted for by the mass polarization correction, of the form

$$E_M = (m/M)\vec{P}_1 \cdot \vec{P}_2.$$

This has been evaluated by APS and by Ermolaev and Jones.[9] The finite nuclear size effect, or volume isotope shift has been evaluated by Kastner.[14] This operator has the form

$$E_N(n, l) = \tfrac{2}{3}\pi Z e^2 \left|u_{nl}(0)\right|^2 \langle r^2 \rangle,$$

where $\langle r^2 \rangle$ is the mean-squared radius of the nuclear charge distribution.

Only the lowest-order QED effects have been explicitly derived for heliumlike atoms. Kabir and Salpeter[16] and Araki[17] have derived the lowest-order term of the form $Z^4\alpha^5$, which is analogous to the hydrogenic shift. The terms of the form $Z^3\alpha^5$ and $Z^3\alpha^5 \ln(\alpha)$ have been derived by Araki[17] and Sucher.[18] The $Z^5\alpha^6$ terms have been estimated by several authors.[19]

Recently, Kastner[14] and Ermolaev[20] have made numerical evaluations of QED effects for high-Z ions. Ermolaev employed a phenomenological treatment to account for two-electron interaction corrections to the self-energy terms. In this way, he included the $1/Z$ corrections, but did not include the $(Z\alpha)$ corrections. From analogy with the hydrogenic QED corrections, the $(Z\alpha)$ corrections have coefficients which are equal to or larger than the lowest order coefficients, and for high-Z ions contribute a major part of the total effect.

The number chosen for the QED contribution is from Erickson's results for hydrogenlike ions.[21] By using these results, terms that are higher order in $(Z\alpha)$ are included approximately, but terms of order $1/Z$, unique to two electron atoms, are neglected.

Table I shows the magnitudes of these various contributions to the $2\,^3P_2$-$2\,^3S_1$ and $2\,^3P_0$-$2\,^3S_1$ energy differences for the case of heliumlike argon. The neglected terms are all estimated to be in the third decimal place. The error quoted is the difference between the QED contribution for the cases

TABLE II. Previous measurements of the $2\,^3P_J \rightarrow 2\,^3S_1$ wavelengths are shown as a function of nuclear charge Z. All values are vacuum wavelengths in angstroms.

	Z	$2\,^3P_2 \rightarrow 2\,^3S_1$	$2\,^3P_1 \rightarrow 2\,^3S_1$	$2\,^3P_0 \rightarrow 2\,^3S_1$	Date	Ref.
He	2	10833.27	10833.27	10833.06	1932	22
Li	3		Resolves hfs		1927	23
			Resolves hfs		1974	24
Be	4	3721.98	3724.04		1934	25
		3721.42 ± 0.1	3723.53 ± 0.1	3721.97 ± 0.1	1972	26
		3721.91 ± 0.03	3723.97 ± 0.03	3722.37 ± 0.3	1973	27
B	5	2822.51	2826.68		1934	25
				2825.40 ± 0.05	1952	28
C	6	2271.59 ± 0.05	2278.63 ± 0.05	2277.96 ± 0.05	1952	28
N	7	1896.82	1907.34	1907.87	1964	29
		1896.83 ± 0.02	1907.34 ± 0.02	1907.80 ± 0.05	1973	30
O	8	1623.29 ± 0.08	1637.96 ± 0.08	1639.58 ± 0.08	1967	31
		1623.63 ± 0.08	1638.30 ± 0.03	1639.87 ± 0.08	1971	32
		1623.50 ± 0.02	1638.25 ± 0.02	1639.90 ± 0.08	1973	30
F	9	1414.42 ± 0.06	1433.82 ± 0.06	1437.07 ± 0.06	1971	32
Ne	10	1248.12 ± 0.02	1272.81 ± 0.04	1277.68 ± 0.04	1971	32
Kr	36			284.0 ± 4.5	1975	33

$Z = 18$ and $Z = 17$. This is roughly three times the estimated size of the $1/Z$ corrections to the QED effects.

B. Previous observations

Table II gives some of the more recent energy measurements of the $2\,^3P_J$-$2\,^3S_1$ energy differences. Note that there are no direct observations beyond $Z = 10$. The result at $Z = 36$ is inferred from the measured lifetime for the $2\,^3P_0$ state.

C. Lifetime calculations

The calculation of lifetimes, or oscillator strengths (f values), has paralleled the work on energy levels. The f values are very sensitive to the wave functions employed, and accurate f values require the use of wave functions of high accuracy. Schiff, Pekeris, and Accad[34] calculated f values for ions with $2 \leq Z \leq 10$, employing the variational wave functions which they had derived.[8] Sandars and Scherr[7] gave $1/Z$ expansions for the f values. Recently, Mohr has given power series expressions for the decay rates, including several of the $1/Z$ corrections to the nonrelativistic hydrogenic approximation, and the lowest-order relativistic correction of order $(Z\alpha)^2$.[35,36]

D. Previous observations

Observed lifetimes for the heliumlike $2\,^3P_J$ states have now been reported through $Z = 36$. The most recent work is shown in Table III. However, beyond $Z = 10$, there have been no reported observations of the $2\,^3P_J$-$2\,^3S_1$ transitions. The $2\,^3P_2$ life-

TABLE III. Recent lifetime measurements of the He-like $2\,^3P_J$ states are shown as a function of nuclear charge Z. All lifetimes are listed in nsec.

Z	$2\,^3P_0 \rightarrow 2\,^3S_1$	$2\,^3P_2 \rightarrow 1\,^1S_0$	Date	Ref.
2	96 ± 11		1963	37
	99 ± 5		1965	38
	105 ± 5		1965	39
	99 ± 8.4		1968	40
3	54.4 ± 2.7		1967	41
	33 ± 2		1969	42
	45 ± 5		1973	43
4	22.3 ± 1.0		1969	44
5	24 ± 4		1970	45
6	16 ± 2		1970	46
	11.4		1970	47
	14 [a]		1971	48
	16.5 [b]		1971	48
7	13.8		1970	47
	13.8		1971	49
8	15.1		1970	47
9	10.2 ± 1.8 [a]		1974	50
	13.3 ± 3.0 [c]		1974	50
10	12.6		1970	47
16		2.5 ± 0.2	1974	51
17		1.86 ± 0.1	1974	52
18		1.7 ± 0.3	1970	53
22		0.44 ± 0.03	1974	54
23		Observed	1974	35
26		0.11 ± 0.02	1974	35
36	1.66 ± 0.06 [c]		1976	33

[a] $^3P_{0,1} \rightarrow {}^3S_1$.
[b] $^3P_2 \rightarrow {}^3S_1$.
[c] $^3P_0 \rightarrow {}^3S_1$.

times have been measured by observing the $M2$ transition to the ground state. For some of the heavier ions, the $2\,^3P_1$ lifetime has been measured by observing the intercombination line to the ground state. The result for $Z=36$ was measured by observing the x ray emitted by the rapidly decaying $2\,^3S_1$ state following the decay of the $2\,^3P_0$ state.

III. EXPERIMENT

A. Apparatus

These experiments were performed at the Lawrence Berkeley Laboratory heavy-ion linear accelerator (Super-HILAC), using the 138.5-MeV argon-ion beam. This beam energy corresponds to an ion velocity of $\beta=0.086$ and exponential $(1/e)$ decay lengths for the $2\,^3P_{2,0}$ states, respectively, of 3.94 and 11.6 cm based on the predicted lifetimes.

The apparatus is shown schematically in Fig. 2. The ion beam emerging from the accelerator was magnetically bent and focused into the beam line. It was collimated by metal collimators located at various points along the beam pipe and then passed through a thin carbon foil ($\approx 50\ \mu g/cm^2$) which excited the states of interest. Downstream of the foil, photons from decays in flight of the foil-excited atoms were observed at 90° to the beam center line with a vacuum ultraviolet monochromator. With charge currents of 500 nA, count rates of 10 counts/sec were observed at the line peaks. The beam atoms were collected in a Faraday cup monitored with a Brookhaven Instrument Corporation SCIF 1000C current integrator. The lifetimes were measured by varying the distance between the exciting foil and the entrance slit of the monochromator.

B. Monochromator

An early production model $\frac{1}{2}$-m Seya-Namioka Vacuum Ultraviolet Monochromator was used in these measurements.[55] This monochromator is a non-Rowland circle instrument, having a compact vacuum vessel with fixed entrance and exit slits, which scans the spectral region by rotating the grating. Figure 2 shows several of the relevant parameters for the instrument. The entrance slit was mounted perpendicular to the beam axis.

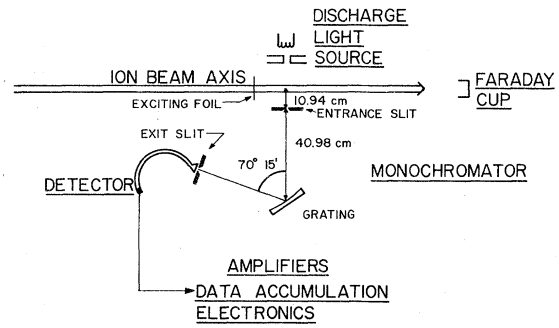

FIG. 2. Schematic view of the apparatus, showing the major parts which are discussed further in the text.

A tripartite replica grating with a ruled area of 30×50 mm (length of grooves × width of ruled area) and having 1200 grooves/mm was used as the dispersive element. The grating was overcoated with platinum, which has a peak reflectivity of ≈20% near 600 Å.[56,57] In the Seya-Namioka mounting the grating has a blaze wavelength of ≈570 Å.

To reduce background noise levels due to scattered light inside the monochromator's vacuum vessel, brass shields were fitted in the entrance and exit arms so the slits only viewed the grating, and not the walls of the vacuum vessel. The monochromator was operated at pressures between 1×10^{-6} and 3×10^{-7} Torr with a liquid-nitrogen-trapped diffusion pump.

To maximize the signal count rates, data were collected with the entrance and exit slits at 200 μm. This gave instrumental linewidths of 3.8 Å, and for $\lambda=600$ Å and $\beta=0.086$ gave angular Doppler widths of 4.8 Å for the 5-cm-wide grating.

C. Discharge light source

A condensed-spark discharge light source was constructed for use in alignment of the monochromator, and determination of a dispersion curve for the instrument. This light source was modeled on a design of Samson.[56] A 0.25-μF capacitor charged to 5–6 kV was discharged across a low-pressure flowing gas which was constrained in a ceramic capillary 5 cm long and 3.5 mm in diameter.

High-purity argon gas exhibits a rich line spectrum below 1000 Å and was used as the flowing gas. We observed many lines in the spectral region from 500 to 700 Å. Twenty resolved lines of Ar IV-Ar VII and impurity lines of O III, O IV, and N III were identified by comparison with spectrographic plates taken of this light source. These lines were then treated as wavelength standards (a good assumption for the accuracy attainable in this work) and were fit to a dispersion curve.

When the 20 spectral lines were fitted by a second-order equation, the points exhibited a periodic oscillation about this dispersion curve. The period of oscillation was equal to one rotation of the precision drive screw in the sine drive mechanism. When this oscillation was fitted with a sine function of fixed period it has an amplitude of 0.1–0.2 Å. This oscillation could be due to an error in the screw, or an improper adjustment of the bearings

in which the drive screw pivoted. When correctly aligned a sine drive gives a linear dispersion curve. This particular instrument had very poor adjustment points and was impossible to align properly. To first order an error in a sine drive is a cosine-type function, describable over a short arc by a second-order equation. To describe the distribution of the reference lines a five-parameter dispersion curve, consisting of second-order equation plus a sine function, was fit to the data.

D. Detector

Individual photons passing through the monochromator were counted with a Bendix Continuous Dynode Electron Multiplier (CDEM), model 4700. The CDEM detector had a background rate of 3–5 counts/min, was solar blind and could be cycled to air with no degradation of performance. CDEM detectors have measured quantum efficiencies of (15–25)% in the spectral range from 500 to 700 Å.[58] To ensure an adequate vacuum for the operation of the detector it was separately pumped by a small liquid-nitrogen-trapped diffusion pump.

High background levels were observed when the accelerator delivered beam to our experimental area. To decrease the background count rate, a lead house with 4-in.-thick walls was assembled around the detector. The detector was also shielded from the Faraday cup which acted as the beam dump.

E. Data-collection electronics

Figure 3 shows a block diagram of the electronics assembled for this experiment. Output pulses from the CDEM were capacitively coupled into very fast amplifiers with a total gain of 600. The output pulses from these amplifiers had pulse heights of ≈0.4 V and were 20–30 nsec long. They were then passed through an ECL discriminator-amplifier, with the discriminator level at 0.1 V, and emerged as TTL level pulses. A special gating box routed these pulses into one of two available data collection devices.

Both data collection systems were multichannel

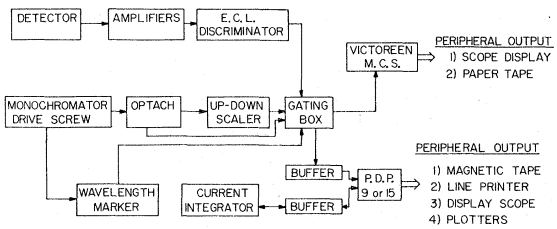

FIG. 3. Block diagram of the electronics and data collection system.

scalers (MCS), which received external start and time-base pulses from the gating box. These pulses were generated by an optical shaft encoder (OPTACH) and an associated UP-DOWN scaler. The OPTACH divided the wavelength spectrum into equal wavelength bins. This was necessary for digital data collection, as the monochromator's drive mechanism, consisting of a precision screw rotated by a geared drive train driven by two differentially coupled continuous motors and three electromagnetic clutches, provided continuous scan rates of 5–1500 Å/min. The OPTACH was coupled to one end of the precision drive screw. One rotation of the screw (which corresponded to advancing the monochromator through 30 Å) was divided into 500 equal wavelength bins. Additionally, the OPTACH allowed sensing the direction of rotation of the drive screw. The UP-DOWN scaler recorded the amount of rotation of the drive screw and provided an external indication of the operation of the drive mechanism.

The MCS start pulse was generated when the UP-DOWN scaler crossed zero as it was counting up (or scanning toward longer wavelengths). Mechanical problems associated with the monochromator could cause a loss or gain of counts in the UP-DOWN scaler when the scanning was stopped and reversed in direction. To overcome this problem a set of electronic gates was constructed, all switch contacts were bypassed, and some unnecessary parts were removed from the drive mechanism. To fully circumvent this problem a wavelength-marker system was constructed. Four mirrors were mounted on one end of the drive screw. A laser was positioned to bounce light off these mirrors onto a phototransistor, and thereby generate pulses at certain points during the rotation of the drive screw. If these points did not duplicate from scan to scan, it was assumed the electronics had erred, and the data was adjusted accordingly.

With this system the wavelength spectrum was scanned at 5 Å/min and counts were accumulated in each wavelength bin for roughly 0.6 sec. For normalization purposes the amount of beam current entering the Faraday cup was recorded for each wavelength bin. This normalization procedure is important since during the scanning time of a spectral line (about 3 min) there were fluctuations in the ion beam current. Moreover, nonlinearities in the gear system which drove the precision screw caused large variations in the amount of time the monochromator looked at each equal wavelength bin.

The PDP computer system was programmed to act as four parallel 512 channel MCS. The first MCS stored the number of counts recorded during each wavelength bin. The second MCS stored the

wavelength marker points. The third MCS stored a coded word corresponding to the beam current reading of the BIC SCIF Current Integrator. After each spectral scan these three MCS spectra were stored on magnetic tape for later data analysis. The fourth MCS was a cumulative sum of the first MCS spectra so the unnormalized line shape could be observed growing in the time during data collection.

The Victoreen 8600 MCS was a single multichannel scaler, and therefore was not able to collect all the necessary data for this experiment. It had a faster count rate capability (modified to ≈30 MHz) than the PDP system (<1 MHz) and was used to collect the reference spectra from the condensed discharge lamp. This lamp produced very intense radiation in 1-μ sec pulses, mimicking count rates in excess of 1 MHz.

IV. EXPERIMENTAL RESULTS

Since earlier work had shown that the $2\,^3P_2$ level was populated, we initially searched for the transition $2\,^3P_2$-$2\,^3S_1$. After initial observation of this transition, subsequent rearrangement of the apparatus and improved shielding enhanced the signal-to-noise rate.

To optimize the observational parameters as a function of ion beam velocity, observations were made for beam energies in the range 47–340 MeV, corresponding to beam velocities $0.051c$–$0.135c$. These results are shown in Fig. 4. At 47 MeV no signal was observable. The data shown have statistics of 200 counts in the peak bins, and are not normalized for beam-current variations. No effort was made at this time to measure absolute wavelengths.

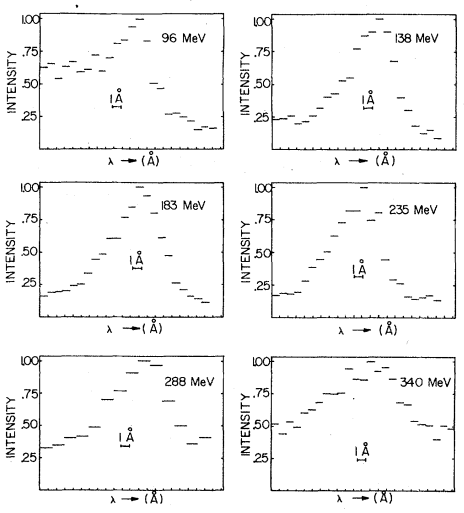

FIG. 4. Observed $2\,^3P_2$-$2\,^3S_1$ line shapes for He-like argon as a function of beam energy. The peaks have typical statistics of 200 counts in the peak bins. The zero points are different for each observation. The absolute wavelength was not measured.

Since lower ion velocities give smaller Doppler widths most subsequent data was taken at a beam energy of 138.5 MeV, or $\beta = 0.086$. A very strong asymmetry is seen on the low wavelength or high-energy side of the $2\,^3P_2$-$2\,^3S_1$ line at a beam energy of 96 MeV. There appears to be a similar asymmetry for observations at higher beam energies, though it is smaller in amplitude relative to the main peak. Insufficient beam time precluded a systematic study of this feature, but more will be said about it later. Finally, the $2\,^3P_0$-$2\,^3S_1$ transition was easily observed. It is broader because of Doppler effects, and was observed with a lower signal count rate.

Charge-state fractions emerging from the exciting foil (50- and 100-μg/cm^2 carbon foils) were measured for the 138-MeV argon-ion beam. A small Faraday cup, not electrostatically suppressed, was monitored by a sensitive electrometer to detect the magnetically dispersed charge states. No noticeable difference was observed for the two foil thicknesses. The results, which must be assigned large errors due to the nonsuppressed Faraday cup, were the following: fully stripped, 8%; one electron, 31%; two electron, 36%; three electron, 19%; four electron, 5%; and very little of lower charge-state fractions.

A. Time-of-flight lifetime results

Lifetimes of the decaying states were measured using a time-of-flight (TOF) technique. The position of a 49-μg/cm^2 carbon foil mounted on a moveable track was varied with respect to the entrance slit of the monochromator. Data were taken in the following manner: The spectral lines were first scanned to locate the line peak. Wavelength points were then selected at two or three positions under the peak, and at two positions in the background, ≳10 Å above and below the peak. Data were collected only at these wavelength points by setting the monochromator at these points and recording the number of counts for a certain amount of integrated beam current. This procedure was repeated for different foil positions.

Using this method it took $7\frac{1}{2}$ h to measure three decay curves for the $2\,^3P_2$-$2\,^3S_1$ decay. Each decay curve consisted of eight data points over a total distance of 6.60 cm. For the $2\,^3P_0$-$2\,^3S_1$ transition two decay curves of 13 data points over a distance of 16.51 cm were measured in 12 h of beam time.

The background count rate was defined as the average of the count rates at the high- and low-

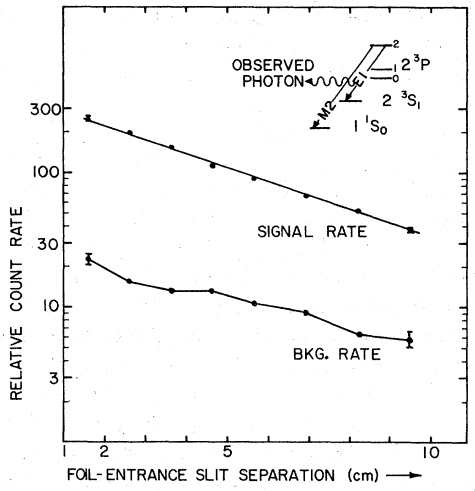

FIG. 5. Measured decay curve for the $2\,^3P_2$-$2\,^3S_1$ transition in He-like argon.

wavelength points. Figures 5 and 6 show the sum of all the data collected for the two decays. The signal count rate has been corrected for the background shown below it in the figures. The straight lines are least-squares fits of single exponentials to the observed data. For the $2\,^3P_0$-$2\,^3S_1$ decay only the last eight data points are fit. The first five data points cause a concave shape in the decay curve for which we have no plausible explanation.

B. Absolute wavelength standards

Accurate measurement of the wavelengths of the heliumlike lines necessitated the use of known spectral lines as wavelength references. Because the Doppler effect both shifts and broadens the

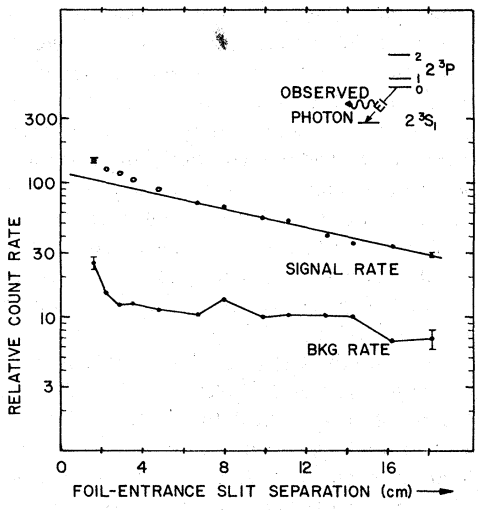

FIG. 6. Measured decay curve for the $2\,^3P_0$-$2\,^3S_1$ transition in He-like argon.

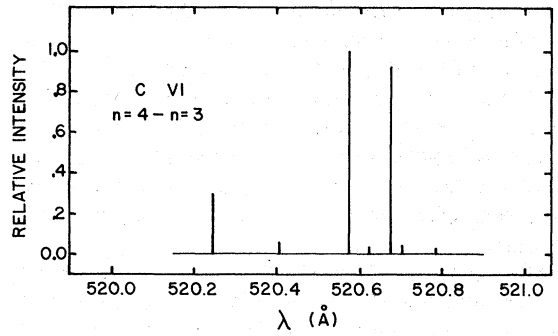

FIG. 7. Theoretical fine structure of the H-like $n=4 \rightarrow n=3$ transition in C VI based on a $(2j+1)$ statistical population of the different j states.

wavelengths of lines emitted by moving light sources it was necessary to use foil-excited lines as the wavelength references.

The Super-HILAC is a very-high-energy machine by comparison with most beam-foil sources, therefore foil-excited beams consist mainly of very highly stripped ions. Well-known lines from laboratory observations are generally from low charge states of ions. This problem was circumvented by noting that wavelengths of hydrogenlike lines can be accurately calculated from the Dirac equation, and should be easily excited by the Super-HILAC.

Calculations were made for possible decays of ions with $Z \leq 18$ which fell in the range of 500–700 Å and for which sources were available at the Super-HILAC. Two possible lines were found, one in hydrogenlike carbon, $n=4 \rightarrow n=3$ near 520 Å, and one in hydrogenlike oxygen, near 632 Å, $n=5 \rightarrow n=4$.

The calculated structure of these lines is shown in Figs. 7 and 8. Tables IV and V list the wavelengths, lifetimes, and intensities based on a $(2j+1)$ statistical distribution of the excited state populations. The intensity distribution is shown schematically in the diagram, and appreciable structure

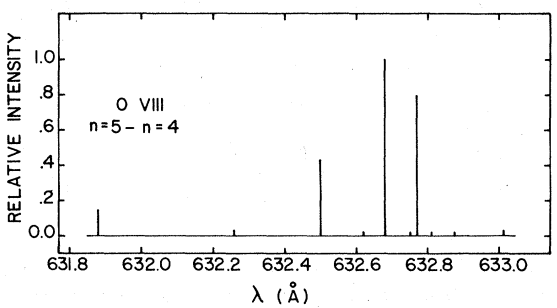

Fig. 8. Theoretical fine structure of the H-like $n=5 \rightarrow n=4$ transition in O VIII based on a $(2j+1)$ statistical population of the different j states.

TABLE IV. Fine structure of H-like carbon line.

Transition	λ (Å)	τ (nsec)	Rel. intensity
$4f\ \frac{7}{2}$-$3d\ \frac{5}{2}$	520.68	0.056	0.922
$4f\ \frac{5}{2}$-$3d\ \frac{3}{2}$	520.58	0.056	0.646
$4d\ \frac{5}{2}$-$3p\ \frac{3}{2}$	520.58	0.028	0.345
$4d\ \frac{3}{2}$-$3p\ \frac{1}{2}$	520.25	0.028	0.197
$4p\ \frac{3}{2}$-$3s\ \frac{1}{2}$	520.25	0.009	0.102
$4p\ \frac{1}{2}$-$3s\ \frac{1}{2}$	520.41	0.009	0.051
$4s\ \frac{1}{2}$-$3p\ \frac{1}{2}$	520.41	0.172	0.010
$4f\ \frac{5}{2}$-$3d\ \frac{5}{2}$	520.71	0.056	0.046
$4s\ \frac{1}{2}$-$3p\ \frac{3}{2}$	520.79	0.172	0.021
$4p\ \frac{1}{2}$-$3d\ \frac{3}{2}$	520.79	0.009	0.005
$4d\ \frac{3}{2}$-$3p\ \frac{3}{2}$	520.63	0.028	0.039
$4p\ \frac{3}{2}$-$3d\ \frac{3}{2}$	520.63	0.009	0.001
$4p\ \frac{3}{2}$-$3d\ \frac{5}{2}$	520.76	0.009	0.010

TABLE V. Fine structure of H-like oxygen line.

Transition	λ (Å)	τ (nsec)	Rel. intensity
$5g\ \frac{9}{2}$-$4f\ \frac{7}{2}$	632.77	0.057	0.795
$5g\ \frac{7}{2}$-$4f\ \frac{5}{2}$	632.68	0.057	0.613
$5f\ \frac{7}{2}$-$4d\ \frac{5}{2}$	632.68	0.034	0.387
$5f\ \frac{5}{2}$-$4d\ \frac{3}{2}$	632.50	0.034	0.271
$5d\ \frac{5}{2}$-$4p\ \frac{3}{2}$	632.50	0.017	0.167
$5d\ \frac{3}{2}$-$4p\ \frac{1}{2}$	631.88	0.017	0.093
$5p\ \frac{3}{2}$-$4s\ \frac{1}{2}$	631.88	0.006	0.055
$5g\ \frac{7}{2}$-$4f\ \frac{7}{2}$	632.81	0.057	0.022
$5d\ \frac{5}{2}$-$4f\ \frac{7}{2}$	632.87	0.017	0.007
$5f\ \frac{5}{2}$-$4d\ \frac{5}{2}$	632.75	0.034	0.019
$5d\ \frac{5}{2}$-$4f\ \frac{5}{2}$	632.75	0.017	0.000
$5p\ \frac{3}{2}$-$4d\ \frac{5}{2}$	632.87	0.006	0.012
$5d\ \frac{3}{2}$-$4f\ \frac{5}{2}$	632.87	0.017	0.006
$5d\ \frac{3}{2}$-$4p\ \frac{3}{2}$	632.62	0.017	0.019
$5p\ \frac{3}{2}$-$4d\ \frac{3}{2}$	632.62	0.006	0.000
$5s\ \frac{1}{2}$-$4p\ \frac{3}{2}$	633.01	0.087	0.016
$5p\ \frac{1}{2}$-$4d\ \frac{3}{2}$	633.01	0.006	0.007
$5p\ \frac{1}{2}$-$4s\ \frac{1}{2}$	632.26	0.006	0.027
$5s\ \frac{1}{2}$-$4p\ \frac{1}{2}$	632.26	0.087	0.008

is present over a wavelength region of ≈0.4 Å. The very short lifetimes meant these decays had to be observed directly after the ions emerged from the exciting foil.

To observe these decays a special foil holder was constructed to hold a foil in the beam center line with the foil surface at an angle of 27° to the beam axis. The grating viewed 1.08 cm of the beam axis, therefore, it saw only the central portion of the ellipse formed by the intersection of the circularly collimated beam (0.794-cm diam) and the foil.

C. Observed lines

Figures 9 and 10 show typical line shapes observed for the hydrogenlike carbon and oxygen lines taken using the tilted foil holder. The solid dots show every other data point and the open circles are a model line shape. These curves are the sum of numerous scans of the lines and the error bars represent the counting statistics at the line peaks. Similarly, Figs. 11 and 12 show typical line shapes observed for the two heliumlike argon lines, $2\,^3P_2$-$2\,^3S_1$ and $2\,^3P_0$-$2\,^3S_1$, respectively. These lines were

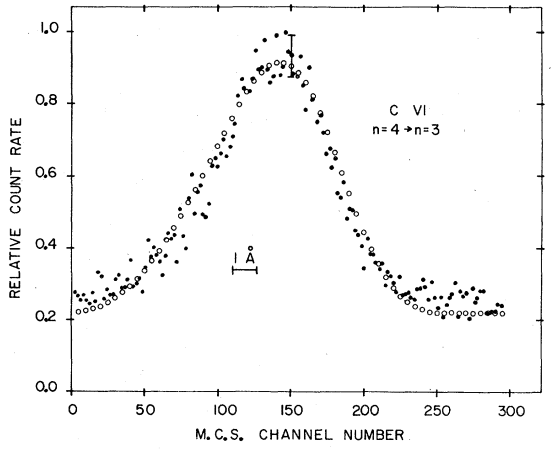

FIG. 9. Data for the H-like $n=4 \rightarrow n=3$ transition in C VI from one data run. The open circles are an empirical fit to the data.

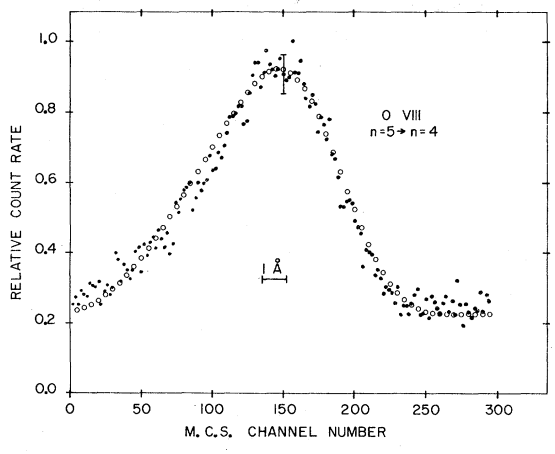

FIG. 10. Data for the H-like $n=5 \rightarrow n=4$ transition in O VIII from one data run. The open circles are an empirical fit to the data.

observed by looking at the decaying atoms downstream from the foil which excited them.

The most striking difference in these four lines is the differing linewidths. The Doppler effect causes linewidths which are dependent on wavelength and velocity. The velocity dependence was eliminated by observing the spectral lines from the three different ion beams, carbon, oxygen, and argon, at beam energies corresponding to the same ion velocity ($\beta = 0.086$).

The linewidth is also dependent on the way the individual spectral lines illuminate the grating. For the heliumlike lines the grating illumination falls off exponentially across the grating, at a rate determined by the lifetime of the excited state. The hydrogenlike lines are observed by looking at the decaying atoms directly as they emerge from the exciting foil, and effects due to the beam shape and the very short lifetimes markedly affect the grating illumination. The grating illumination for a circularly collimated beam of 0.794-cm diam and an excited state lifetime of 0.05 nsec is shown in Fig. 13. Two cases are illustrated. One case assumes a uniform ion density across the beam diameter and the other assumes a Gaussian-density distribution.

During one data run the heliumlike transitions were observed at 96 MeV. The $2\,^3P_2$-$2\,^3S_1$ transition was observed at two different foil-monochromator spacings, one of 0.73 cm and one of 6.70 cm. In both cases the distortion on the high-energy side of the line was visible. Data scans were taken beginning 15 Å below the main peak. The tailing obviously extended further below that point to even higher energies. At the larger separation the only observable change was in the amplitude of the tail. The ratio of the two had decreased, indicating that the tail could be due to the decay of long-lived states.

A scan of the $2\,^3P_0$-$2\,^3S_1$ line was made at this beam energy to see if it was also distorted. Possibly some phenomenon associated with the beam

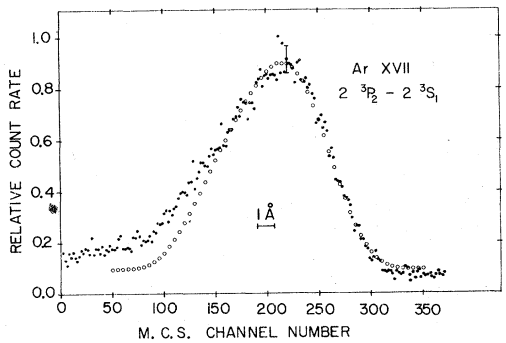

FIG. 11. Data for the He-like argon $2\,^3P_2$-$2\,^3S_1$ transition from one data run. The open circles are an empirical fit to the data, only over channels 170 and above.

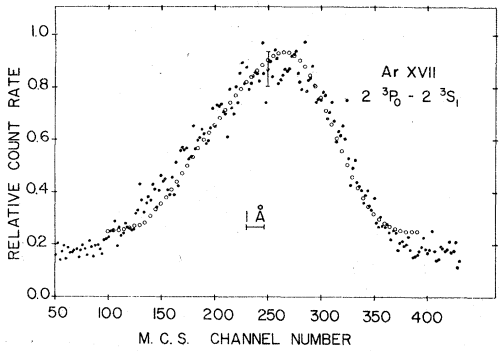

FIG. 12. Data for the He-like argon $2\,^3P_0$-$2\,^3S_1$ transition from one data run. The open circles are an empirical fit to the data.

velocity was affecting the levels. The line looked similar to data taken at beam energies of 138 MeV. It was slightly narrower, possibly due to the lower velocity, and it had a poorer S/N ratio (roughly one to one). The background remained flat and equal on both sides of the observed line.

This test was repeated at a beam energy of 138 MeV, observing both heliumlike lines with a small foil-monochromator separation of 2.19 cm and then with a larger separation of 9.81 or 7.27 cm for the $2\,^3P_0$-$2\,^3S_1$ and $2\,^3P_2$-$2\,^3S_1$ transitions, respectively. There were no distinguishable differences in the linewidths when observed at different foil-monochromator spacings. The S/N ratio was the most obvious difference, going from 3.2 to 1.9 for the $2\,^3P_0$-$2\,^3S_1$ transition and from 14 to 2.5 for the $2\,^3P$-$2\,^3S_1$ transition. The count rates were also considerably lower at the larger separations, and data collection times became very long.

V. DATA ANALYSIS

A. Lifetime data

Using a least-squares procedure, single exponential decay curves were fit to the data. Different weighting functions and background rates were also used in fitting the data, and no appreciable affect was evident in the calculated lifetimes.

The fitting program tested for nonexponential behavior of the decay curves by dropping points from either extreme of the decay curve and refitting the remaining points. The $2\,^3P_0$-$2\,^3S_1$ decay converged to a stable value only after the five points with the shortest foil-monochromator spacing were dropped.

To extract a lifetime from the measured decay rates it was necessary to know the beam velocity. The accelerator has a calculated beam energy of 138.5 MeV and the crystal energy measurement system gave an energy of 143 MeV. Since in general all energy measurements at the Super-HILAC agree within ± 5%, the average of these two num-

bers was used as the beam energy. The foil thicknesses were measured by the manufacturer,[59] and range energy tables were consulted to determine the energy loss upon passage through the foil.[60]

B. Wavelength data

The wavelength-determination data were accumulated and analyzed in the following manner. Scans of the discharge light source were taken from 500–700 Å at the start and finish of each experimental run. During the run the four different foil-excited lines were observed. The line centers were determined from a model line shape fit to the experimental data. The two hydrogenlike lines were then used to calibrate the dispersion curves measured by the discharge light source, and thereby determine the wavelength of the heliumlike transitions.

An important part of this analysis was the model line shape which was fit to the observed data. The line-shape model was empirically constructed to account for the four following effects: (i) the finite excited state lifetimes; (ii) effects due to beam geometry; (iii) effects due to 200-μm-wide monochromator slits; and (iv) Doppler effects. Parts (i) and (ii) were discussed previously. A Gaussian distribution of ions across the beam diameter will manifest itself in (ii), and is expected for an accelerator of this type. Since we were unable to measure this parameter, and the location of the apparatus with respect to the beam focusing elements would tend to average out this property, we assumed the beam density was uniform.

Figure 14 shows the line shape recorded with the monochromator viewing the 584-Å He I line excited by a Hinteregger lamp. The solid dots represent the observed line shape for 200-μm-wide entrance and exit slits. The lamp was mounted so it

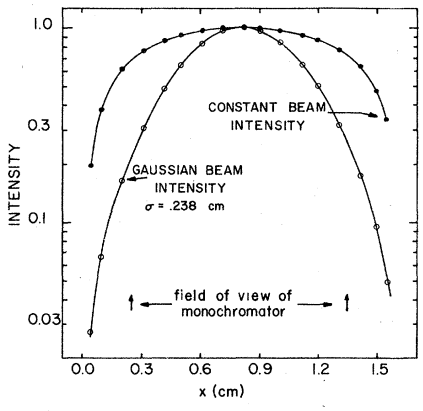

FIG. 13. Theoretical grating illumination by the hydrogenic foil-excited lines. The figure shows curves for two different ion-beam density distributions.

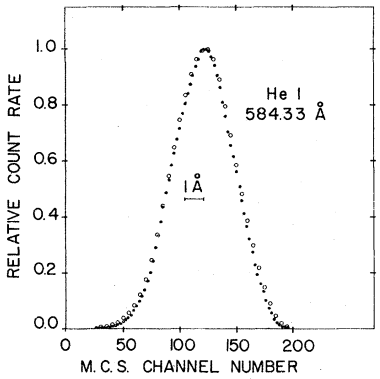

FIG. 14. Data from one scan of the He line at 584 Å excited by a Hinteregger lamp. The open circles are the empirically constructed fit to this data.

illuminated at least 90% of the grating fairly uniformly.

The grating was then modeled as ten separate gratings, each 0.5 cm wide, stacked side by side. Using a pair of bilateral slits and the Hinteregger lamp a line shape was determined for each of these ten "gratings." To model the foil-excited lines, each of the ten line shapes was weighted according to the illumination of that part of the grating, and was shifted an appropriate wavelength increment to account for the angular Doppler effect. The ten line shapes were then added to generate the empirically constructed line shapes.

There are only two possible tests of this model. One is its ability to reproduce the stationary source line shape, the results of which are shown by the open circles in Fig. 14. The other test is how well it reproduces the observed foil-excited lines. This is shown by the open circles in Figs. 9–12. To fit these line shapes to the data we assumed the empirically constructed line shapes were the true line shapes, added a flat background, and used a least-squares routine to determine the best fit.

The fit of the two hydrogenlike lines is very good. The fit of the $2\,^3P_0$-$2\,^3S_1$ line is slightly narrower than the data, and more will be said later about the $2\,^3P_2$-$2\,^3S_1$ fit shown in Fig. 11. This fit was only done over the points above channel number 170.

The hydrogenlike fits shown assume population distributions of the excited states based on a $(2j+1)$ statistical distribution. We also constructed and fit line shapes to the hydrogenlike lines assuming the decays were due only to the states of maximum l and j. This produced variations in the final results which were well within other error limits.

Figure 15 shows the results of several scans of the $2\,^3P_2$-$2\,^3S_1$ transition. These scans were started

at a much lower wavelength point than the previous data. The triangles represent a single line fit to the data over channels 300–495. The open circles are the results of a two line fit to the data. This fit centered the main peak only one channel from where the single peak was fit, and centered the second peak at channel 231. This two peak fit seems to describe the data better, but is only satisfactory if a reasonable transition can be found which could be responsible for the decay.

Hydrogenlike decays were investigated using the Dirac equation. The proper energies could be generated only by using $\Delta n > 1$ transitions. Several attempts were made to observe the $n = 8 \rightarrow n = 7$ transition near 588 Å in hydrogenlike argon, with no success.

Heliumlike states were also investigated with no success. There are recent reviews of doubly excited states of heliumlike atoms, both experimental[61] and theoretical.[62] Doyle gives energy calculations for some of these states, as well as for lithiumlike and berylliumlike atoms.[12] These results are supplemented with $1/Z$ energy-expansion calculations.[63] None of the low-lying levels of these ions generate interfering lines.

Doubly excited lithiumlike states have been observed, especially the $1s2s2p\,^4P_{5/2}$ state which has a lifetime of 0.66 ± 0.04 nsec in lithiumlike argon.[64] In the light lithiumlike ions, transitions between the $1s2pnd\,^4D^o$ and $1s2snd\,^4D^e$ states have been observed.[65] These decays appear to fall on the high-energy side of the $1s2p\,^3P$-$1s2s\,^3S$ transitions, but have very short lifetimes and are weak transitions.

The charge-state fraction measurements indicated that only atoms with four or less electrons were abundant in the ion beam. Since we cannot find transitions within these few-electron ions which might correspond to the observation, we have to consider this explanation as suspect. We note however, that the location of the main peak is little affected by whether we assume there is one line, or try to fit two "lines" to the data.

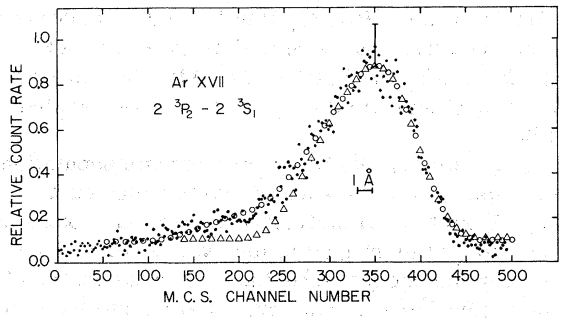

FIG. 15. Data for the He-like argon $2\,^3P_2$-$2\,^3S_1$ transition from one data run. The triangles and circles represent, respectively, a single and double peak fit to the data, as described in the text.

VI. COMPARISON OF EXPERIMENT AND THEORY

A. TOF data

The final results from the lifetime determination are shown in Table VI. Theoretical results calculated using the work referenced in Sec. II are shown for comparison. The theoretical results are shown with and without including the radiative contributions to the energy differences.

The errors quoted for the experimental results are the algebraic sum of the fitting error and a 6% uncertainty in the beam energy. Errors due to the positioning of the moveable foil, energy loss in the foil, and shifts in the electronics or monochromator are all calculated to be well under the 1% level.

B. Wavelength data

To determine the wavelength values the data was fit in several different ways. The two different models used for the hydrogenlike line shapes—one assuming a single component and one assuming a distribution based on $(2j+1)$ statistics—were used to determine the line centers. The line centers determined in this way were then fit to the two dispersion curves to check for consistency. Fairly good consistency was obtained when the hydrogenlike lines were modeled by the $(2j+1)$ statistical model. Much poorer consistency was obtained for the single-component fit.

The major experimental difficulty was associated with the reproducibility of the monochromator. After corrections were made for the gain or loss of channels due to the electronics, there was still a large shift (≈0.6–0.8 Å) between dispersion curves taken before and after the run. This was a problem which occurred throughout the experiment and which we were unable to correct or to understand. The instrument was adjusted as well as possible, all pivot points were tightly clamped, and every effort was made to avoid touching the monochromator during the experimental runs. Nevertheless these types of unpredictable shifts continued, and were the limit on our accuracy.

TABLE VI. Observed and predicted lifetimes ($2\,^3P$-$2\,^3S_1$) of Ar XVII (nsec).

	$2\,^3P_2$-$2\,^3S_1$	$2\,^3P_0$-$2\,^3S_1$
Observed	1.62(8)	4.87(44)
Predicted [a] without Lamb shift	1.50(4)	4.68(12)
Predicted [a] with Lamb shift	1.52(4)	4.80(12)

[a] References 35 and 36, with energies from Sec. II.

TABLE VII. Observed and theoretical wavelengths, Ar XVII.

	Experiment (Å)	Theory [a] (Å)
2^3P_0-2^3S_1	660.7 ± 1.1	662.0 ± 1.1
2^3P_2-2^3S_1	560.2 ± 0.9	560.0 ± 0.9

[a] See discussion in Sec. II.

Because the monochromator gave nonreproducible data, we were unable to say one way of fitting the data was better than another, and we settled on using an average. The final values were determined as the average of the two extreme values determined by the different fitting schemes. The final results are shown in Table VII, along with the theoretical results which were discussed in Sec. II.

The errors were fixed by requiring that they encompass all of the different results obtained from the fitting procedure, plus another 0.2 Å. Uncertainties in the beam velocity, the dispersion curve, and even in the line-shape model were all overwhelmed by the problems with the monochromator's nonreproducible performance.

ACKNOWLEDGMENTS

Many people and support groups have made this work possible. We thank the staff of the Super-HILAC for their work on the development of partial energy ion beams and for delivering three different ion beams during most data runs. We thank A. Ghiorso for the use of his computer facilities. Engineering help was provided by D. MacDonald and W. Harnden.

[1]H. Kayser, *Handbuch der Spectroscopie* (S. Hirzel, Leipzig, 1910), Vol. 5, p. 508.
[2]For example, see K. B. MacAdam, and W. H. Wing, Phys. Rev. A 12, 1464 (1975); 13, 2163 (1976).
[3]S. Bashkin and J. O. Stoner, *Atomic Energy Levels and Grotrian Diagrams 1* (North-Holland–American Elsevier, New York, 1975).
[4]W. Heisenberg, Z. Phys. 39, 499 (1926).
[5]M. L. Lewis, P. H. Serafino, and V. W. Hughes, Phys. Lett. 58A, 125 (1976).
[6]F. M. J. Pichanick, R. D. Swift, C. E. Johnson, and V. W. Hughes, Phys. Rev. 169, 55 (1968); S. A. Lewis, F. M. J. Pichanick, and V. W. Hughes, Phys. Rev. A 2, 86 (1970); A. Kponou, V. W. Hughes, C. E. Johnson, S. A. Lewis, and F. M. J. Pichanick, Phys. Rev. Lett. 26, 1613 (1971).
[7]F. C. Sandars and C. W. Scherr, Phys. Rev. 181, 84 (1969).
[8]Y. Accad, C. L. Pekeris, and B. Schiff, Phys. Rev. A 4, 516 (1971), and earlier work referred to therein.
[9]A. M. Ermolaev, and M. Jones, J. Phys. B 7, 199 (1974).
[10]P. Mohr (private communication).
[11]H. A. Bethe and E. E. Salpeter, *Quantum Mechanics of One- and Two-Electron Atoms* (Springer-Verlag, New York, 1957).
[12]H. T. Doyle, *Advances in Atomic and Molecular Physics* (Academic, New York, 1969), Vol. 5, p. 337.
[13]A. M. Ermolaev and M. Jones, J. Phys. B 5, L225 (1972).
[14]S. O. Kastner, Phys. Rev. A 6, 570 (1972).
[15]B. Schiff, Y. Accad, and C. L. Pekeris, Phys. Rev. A 8, 2272 (1973).
[16]P. K. Kabir and E. E. Salpeter, Phys. Rev. 108, 1256 (1957).
[17]H. Araki, Prog. Theor. Phys. 17, 619 (1957).
[18]J. Sucher, Phys. Rev. 109, 1010 (1958).
[19]E. E. Salpeter and M. H. Zaidi, Phys. Rev. 125, 248 (1962); K. S. Suh and M. H. Zaidi, Proc. R. Soc. Lond. A 291, 94 (1965); A. M. Ermolaev, Phys. Rev. Lett. 34, 380 (1975).
[20]A. M. Ermolaev, Phys. Rev. A 8, 1651 (1973).
[21]G. Erickson (private communication).
[22]W. F. Meggers and G. H. Dieke, J. Res. Natl. Bur. Stand. (U.S.) 9, 121 (1932).
[23]H. Schuler, Z. Phys. 42, 487 (1927).
[24]R. Bacis and H. G. Berry, Phys. Rev. A 10, 466 (1974).
[25]B. Edlen, Nova Acta Reg. Soc. Sci. Ups. (IV) 9, No. 6 (1934).
[26]M. Eidelsberg, J. Phys. B 5, 1031 (1972).
[27]B. Lofstrand, Phys. Scripta 8, 57 (1973).
[28]B. Edlen, Ark. Fys. 4, 441 (1952).
[29]K. Bockasten, R. Hallin, K. B. Johansson, and P. Tsui, Phys. Lett. 8, 181 (1964).
[30]S. C. Baker, J. Phys. B 6, 709 (1973).
[31]R. C. Elton, Astrophys. J. 148, 573 (1967).
[32]W. Engelhardt and J. Sommer, Astrophys. J. 167, 201 (1971).
[33]R. Marrus and H. A. Gould, Bull. Am. Phys. Soc. 20, 818 (1975).
[34]B. Schiff, C. L. Pekeris, and Y. Accad, Phys. Rev. A 4, 885 (1971).
[35]H. Gould, R. Marrus, and P. J. Mohr, Phys. Rev. Lett. 33, 676 (1974).
[36]P. J. Mohr, *Beam Foil Spectroscopy*, edited by I. A. Sellin and D. J. Pegg (Plenum, New York, 1976), Vol. 1, p. 97.
[37]P. J. Kindlmann and W. R. Bennett, Jr., Bull. Am. Phys. Soc. 8, 87 (1963).
[38]W. R. Bennett, Jr., P. J. Kindlmann, and G. N. Mercer, Appl. Opt. Suppl. 2, 34 (1965).
[39]J. Lifsitz and R. H. Sands, Bull. Am. Phys. Soc. 10, 1214 (1965).
[40]D. A. Landman, Phys. Rev. 173, 33 (1968).
[41]J. P. Buchet, A. Denis, J. Desequelles, and M. Dufay, C. R. Acad. Sci. (Paris) 265B, 471 (1967).
[42]W. S. Bickel, I. Martinson, L. Lundin, R. Buchta,

J. Bromander, and I. Bergstrom, J. Opt. Soc. Am. 59, 830 (1969).
[43]A. Adler, W. Kahan, R. Novick, and T. Lucatorto, Phys. Rev. A 7, 967 (1973).
[44]T. Andersen, K. A. Jessen, and G. Sorensen, Phys. Rev. 188, 76 (1969).
[45]I. Martinson, W. S. Bickel, and A. Olme, J. Opt. Soc. Am. 60, 1213 (1970).
[46]I. Martinson and W. S. Bickel, Phys. Lett. 31A, 25 (1970).
[47]M. Dufay, A. Denis, and J. Desesquelles, Nucl. Instrum. Meth. 90, 85 (1970).
[48]M. C. Poulizac, M. Druetta, and P. Ceyzeriat, J. Quant. Spectrosc. Radiat. Transfer 11, 1087 (1971).
[49]J. Desequelles, Ann. Phys. (Leipz.) 6, 71 (1971).
[50]J. R. Mowat, P. M. Griffin, R. S. Peterson, H. H. Haselton, R. Laubert, D. J. Pegg, R. S. Thoe, and I. A. Sellin, Bull. Am. Phys. Soc. 19, 468 (1974).
[51]C. L. Cocke, B. Curnutte, and R. Randall, Phys. Rev. A 9, 1823 (1974).
[52]C. L. Cocke, B. Curnutte, J. R. Macdonald, and R. Randall, Phys. Rev. A 9, 57 (1974).
[53]R. Marrus and R. W. Schmieder, Phys. Rev. Lett. 25, 1689 (1970); Phys. Rev. A 5, 1160 (1972).
[54]H. Gould (private communication).
[55]M. Seya, Sci. Light (Tokyo) 2, 8 (1952); T. Namioka, *ibid.* 3, 15 (1954); H. Greiner and E. Schaeffer, Optik 14, 263 (1957); 15, 51 (1958).
[56]J. A. R. Samson, *Techniques of Vacuum Ultraviolet Spectroscopy* (Wiley, New York, 1967).
[57]G. F. Jacobus, R. P. Madden, and L. R. Canfield, J. Opt. Soc. Am. 53, 1084 (1963); E. M. Reeves and W. H. Parkinson, *ibid.* 49, 593 (1959).
[58]M. C. Johnson, Rev. Sci. Instrum. 40, 311 (1969).
[59]Arizona Carbon Foil Co., 415 E. 6th St., Tucson, Ariz. 85711.
[60]L. C. Northcliffe and R. F. Schilling, Nucl. Data A 7, 233 (1970).
[61]H. G. Berry, Phys. Scripta 12, 5 (1975).
[62]E. Holoien, Nucl. Instrum. Meth. 90, 229 (1970).
[63]For helium, see G. W. F. Drake and A. Dalgarno, Phys. Rev. A 1, 1325 (1970); H. Doyle, M. Oppenheimer, and G. W. F. Drake, *ibid.* 5, 26 (1972); G. W. F. Drake, *ibid.* 5, 614 (1972); G. W. F. Drake, and A. Dalgarno, Proc. R. Soc. A 320, 549 (1971): for lithium, see J. S. Onello, L. Ford, and A. Dalgarno, Phys. Rev. A 10, 9 (1974); J. S. Onello, *ibid.* 11, 743 (1975): for beryllium, see D. K. Watson, S. V. O'Neil, *ibid.* 12, 729 (1975).
[64]I. A. Sellin, D. J. Pegg, and P. M. Griffin, Phys. Rev. Lett. 28, 1229 (1972).
[65]H. G. Berry, Phys. Scripta 12, 5 (1975), and references therein; K. X. To, E. J. Knystautas, R. Drouin, and H. G. Berry, *Beam Foil Spectroscopy*, edited by I. A. Sellin and D. J. Pegg (Plenum, New York, 1976), Vol. 1, p. 385; E. J. Knystautas and R. Drouin, *ibid.*, Vol. 1, p. 393.